Journal Pre-proof

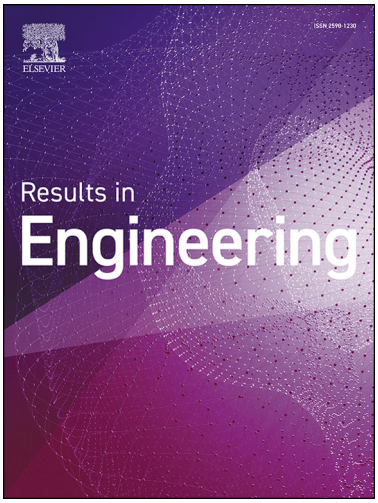

Multivariate regression analysis for rapid fatigue prediction in airport rigid pavements

Luca Bianchini Ciampoli, Ruggero Pinto and Andrea Benedetto

PII: S2590-1230(25)02031-6
DOI: https://doi.org/10.1016/j.rineng.2025.105959
Reference: RINENG 105959

To appear in: *Results in Engineering*

Received date: 9 May 2025
Revised date: 18 June 2025
Accepted date: 23 June 2025

Please cite this article as: L.B. Ciampoli, R. Pinto and A. Benedetto, Multivariate regression analysis for rapid fatigue prediction in airport rigid pavements, *Results in Engineering*, 105959, doi: https://doi.org/10.1016/j.rineng.2025.105959.

Highlights

- Proposed stress and damage model estimates residual life at pavement measurement scale.
- Traditional stress theories underperform compared to advanced numerical simulations.
- Regression on Westergaard's formulas enables rapid, closed-form stress calculations.
- Mechanistic–empirical method links tensile stress directly to cumulative fatigue damage.
- Model improves APMS accuracy, aligning design and monitoring for better decision-making.

Multivariate regression analysis for rapid fatigue prediction in airport rigid pavements

Luca Bianchini Ciampoli[a,*], Ruggero Pinto[a], Andrea Benedetto[a]

[a]*Department of Civil, Computer Science and Aeronautical Technologies Engineering, Roma Tre University, Via Vito Volterra 62, Rome, 00146, Italy*

Abstract

The Airport Pavement Management System (APMS) of extensive air - side infrastructures demands a continuous measurement survey, up-to-date monitoring analysis, proactive rehabilitation and maintenance strategy. Reactive management protocols and current lack of integration in design, survey, and monitoring procedures undermine the effectiveness of any long-term decision making processes. In particular, rigid pavement are currently designed with numerical models and subsequently surveyed with NDT techniques as plate elementary units. Due to the high computational times and numerical resources required, FEA analyses are typically averaged on representative sample units, which inhibits the reliability of the assessment procedure. On the other hand, the use of theoretical closed-form solutions simplifies the physical model allowing for rapid evaluation, at the expense of overall accuracy. In this study, numerical solutions are taken as a reference for setting up a multivariate regressive analysis of rapid theoretical models, with varying pavement and traffic conditions. Hereby, a mechanistic-empirical fatigue condition assessment is directly established and validated to automatically infer Cumulative Damage Factor (CDF) calculation from previous tensile stress results. Relevant results demonstrate a good viability of the proposed method against current stress calculation and damage prediction models, thereby showing potential to contribute to the existing APMS frameworks.

Keywords: Pavement Management System, Concrete Pavement, APMS, Stress Field Analysis, Bottom-Up Fatigue Damage, CDF

*Corresponding author

Email address: luca.bianchiniciampoli@uniroma3.it (Luca Bianchini Ciampoli)

Contents

1. Introduction

1.1. APMS insights

Safety, operability, and durability standards represent crucial concerns in monitoring and management of airport infrastructures. The uncertainty derived from superstructural behaviour and loads applied over time demands a coherent Airport Pavement Management System (APMS) to effectively guarantee ground and air safe operations to the aircrafts. According to the

FAA Advisory Circular [1], an APMS is a systematic procedure including different phases:

1. survey of pavement properties and measurement of load conditions;
2. decaying performance and service life prediction models;
3. life-cycle cost-benefits analysis over curative and/or predictive maintenance interventions;
4. decision making based on optimal resource allocation and efficiency management policies.

Over time, various experiences with APMS applications have been reported as successful in providing asset managers with a large-scale coarse information about the condition of paved areas ([2]; [3]; [4]). However, despite being the only regulated macro-scale tool to handle airside infrastructures, an APMS often struggles to accurately assess the integrity of the paved asset handled [5], due to the:

- lack of effective management and integration of mechanical and geometrical survey data for residual service life prediction purposes [6];
- reliance on reactive and long-term ineffective monitoring and maintenance policies [7].

Such issues are particularly evident in the specific case of apron stands, in which surveying the structural properties of the inherent rigid pavement is a major concern. Unexpected fatigue crack failure can force the airport manager to close the facility, exposing the airport to air traffic capacity problems during the concrete casting and maturation time required by pavement renewal, especially without adequate countermeasures planned.

1.2. Rigid pavement management

At the present state-of-the-art, rigid pavements are designed as theoretical multilayer elements engineered to withstand the expected air-traffic mix. Rigid superstructures generally comprise a first main load-bearing layer (unreinforced concrete, typically) and an intermediate layer (in cement-treated crushed aggregates, usually) laid over the subgrade. The intrinsic stiff properties of these construction materials combined with the high magnitude of the quasi-static bending loads approximate the behavior of rigid pavement to elastic solids, which allows for a remarkable simplification of the physical model, but, on the other hand, requires periodic measurement of mechanical

properties (namely, elastic module E, Poisson coefficient ν) and geometrical configuration (i.e., layer thicknesses) for the approximation to be sufficiently reliable. Most accountable physical models are based on Westergaard's theories (8; 9) and their subsequent developments. Particularly, Eisenmann's and Thomlinson's [10] are very well-known equations for the calculation of mechanical and thermodynamic stress fields, respectively.

As the physical model struggles to account for complex load applications, such as those exerted by multiple-wheel aircraft gears, equivalence coefficients have been empirically proposed to reconduct these conditions to an Equivalent Single Wheel Load (ESWL) [10] that complies with Westergaard's base assumptions and, thereby, allows for the application of such synthetic modeling.

The monitoring techniques adopted in APMS convey the surveyed data into a mechanistic analysis, applied at the scale of a representative pavement sample unit, namely, a set of concrete slabs. In these regards, significant scientific advancements have been achieved in recent decades in increasing the efficiency of data monitoring and collection, while raising the accuracy of mechanical modeling of the pavement and multiple load interactions. On the one hand, the use of Non-destructive Testing (NDT) and Remote Sensing methods has been widely acknowledged as a means of gathering rapid survey information on the physical condition and mechanical response of the pavement ([7]; [11]; [12]). Among the others, most spread techniques with relevant fields of application in APMS have been synthetically listed in Table 1.

Application	**NDT method**	**Reference**
Layer thickness and cracking, moisture, corrosion and deep distresses	GPR	[13]; [14]; [15]; [16]
Vertical deflection, bearing capacity, layer elastic module, deep distresses	FWD, HWD	[17]; [18]; [19]; [20]
Vertical displacements and subsidence	InSAR	[21]; [22]
Superficial distresses and moisture content	Spectral, RGB, IRT Imaging	[23]; [24]
Superficial distresses, geometric configuration	LiDAR	[25]; [26]

Table 1: Main use of NDT and Remote Sensing in rigid pavements assessments

However, limitations in accuracy derived from both the physical approximation of the pavement to an elastic solid and the use of equivalent loads have been successfully overcome by adopting numerical approaches based on

finite element analysis (FEA) [9], typically run by ad hoc software. Important research efforts have been paid to demonstrate the reliability of FEA in determining the general mechanical behavior of these layered media loaded by exactly-modeled aircraft gears, as shown in further detail in Table 2.

Application	**FEA environment**	**Reference**
Finite 2-D plate pavement simulation	KENSLAB, ILLISLAB	[10]; [27]
Finite 3-D brick pavement simulation	EVERFE, FEAFAA	[28]; [29]
Finite 3-D brick pavement design and residual life	FAARFIELD, ANNFAA	[30]; [31]

Table 2: Main use of FEA in rigid pavements assessments

1.3. Gap in knowledge

Despite the huge evidence for robustness and reliability of FEA techniques in design procedures, open challenges remain, limiting the applicability of these evaluations in high-productive large-scale protocols. In particular, due to computational demand, Ioannides and Donnelly [32] stated that it may be difficult to adopt FEA for mechanical simulations conducted at the elementary unit, i.e., concrete slab. In addition, such algorithms often run on closed-source software that inhibit the procedure from being repeated at the local scale and specific material properties. This involves the simulations to be generally performed on pavement scenarios considered representative of the paved area, thereby contributing to the potential misleading of local maintenance and rehabilitation prioritization.

Hybrid combinations of FEA and closed-form solutions have also been explored [43], verifying the plate-soil nonlinearity interaction with a rapid parametric solution on varying subgrade stiffness loaded with two commercial aircraft. Moreover, Mathi and Nallasivam [40] have tested a modified Westergaard's method on two air traffic loads to study the influence of the elastic modulus of a concrete plate and thickness on the bottom tensile edge and interior stress distributions. Although these rapid approaches in the literature lack to account for richer aircraft databases and pavement properties, both methodologies rely on testing the effect of physical variables through numerical results.
Conversely, the first FEA-reliant machine learning [47] and artificial intelligence [31] efforts to rigid pavement stress prediction models have proven

successful results on extremely large simulation datasets. However, these algorithms, by definition, struggle to explain the physical influence of various pavement characteristics and loading conditions. In addition, these are proprietary models not available to external users.

According to its definition [33], an APMS is expected to ultimately calculate a CDF for each functional unit monitored, based on survey data and expected traffic. However, to rely on quality results in acceptable computing times, stress fields are generally calculated by FEA at the scale of sample units, i.e. a group of 20 slabs, approximatively. Being the mechanical behavior averaged over space, the effectiveness of subsequent cumulative damage prediction models may be locally undermined, thereby leading to potential misestimate in the prioritization hierarchy.

In this sense, there is currently a gap-in-knowledge in CDF direct calculation, which generally limits to the pavement monitoring and inventory only. The calculation of bottom-up fatigue damage is driven by the computation of bottom tensile stresses developed at the base of the concrete layer due aircraft's static bending loads. Being the mechanical behaviour averaged as functional units of analysis on indirect structural parameters' measurement, additional degree of uncertainty in measurement must be accounted as well towards CDF calculation.

Accordingly, this work explores the feasibility of a statistical method that combines the lightness of theoretical-based design models together with the accuracy of FEA in order to set up a FEA validated health assessment protocol suitable for local-scale evaluation even in large, concrete paved areas, such as aprons and holding bays.

2. Methodology

By integrating the inputs of annual traffic mix and pavement properties of each fundamental unit, a unique CDF parameter can be assigned to each specific pavement unit of measurement for which the relevant static stress field is known. This would involve the maintenance and rehabilitation prioritization hierarchy to be actually drive by survey data, thereby representing a further step towards an effective and extensive strategy of proactive maintenance and management of the paved asset.

With the aim of proposing a method based on rapid theoretical equations for determining a CDF remaining service life parameter per individual rigid pavement unit through survey data, the methodology shown in Figure 1 has been adopted and listed hereafter.

- A set of pavement geometrical and mechanical properties is selected, whereas a dataset of aircraft gear loads is collected. These input data are used to generate a number of simulation scenarios.
- The Westergaard's applicability is hence evaluated against equivalent numerical outputs. This comparison assesses the actual attitude of the simplified elastic theory to account for non-linear rigid pavement behaviors.
- A multivariate regression prediction model is run on Westergaard's solutions over FEA results, taken as reference for the various pavement and loading conditions.
- The multivariate model is then tested over a different aircraft dataset for validation purposes.
- Lastly, this rapid tensile predicition model drives an automatic bottom-up fatigue cumulative damage factor algorithm for each aircraft configuration, potentially up datable by survey routines.

3. Input data

On the analysis scale, a coherent stress analysis can be achieved by updating external loads and the geometrical and mechanical response of the rigid pavement.

3.1. Air–Traffic Mixture Characterisation

The breakdown of the operating air-traffic mix is to acknowledge the magnitude and point of application of static loads on the rigid superstructure over its remaining service life. Each aircraft in the spectrum of interest differs in annual traffic distribution, gear geometric configuration, and wheel-track mechanical force applied as specifically published by aircraft manufacturers in technical manuals. The total static load cycle exerted on the area of application by n coverages of i^{th} airplane is measured in terms of magnitude, frequency, and distribution by the following properties:

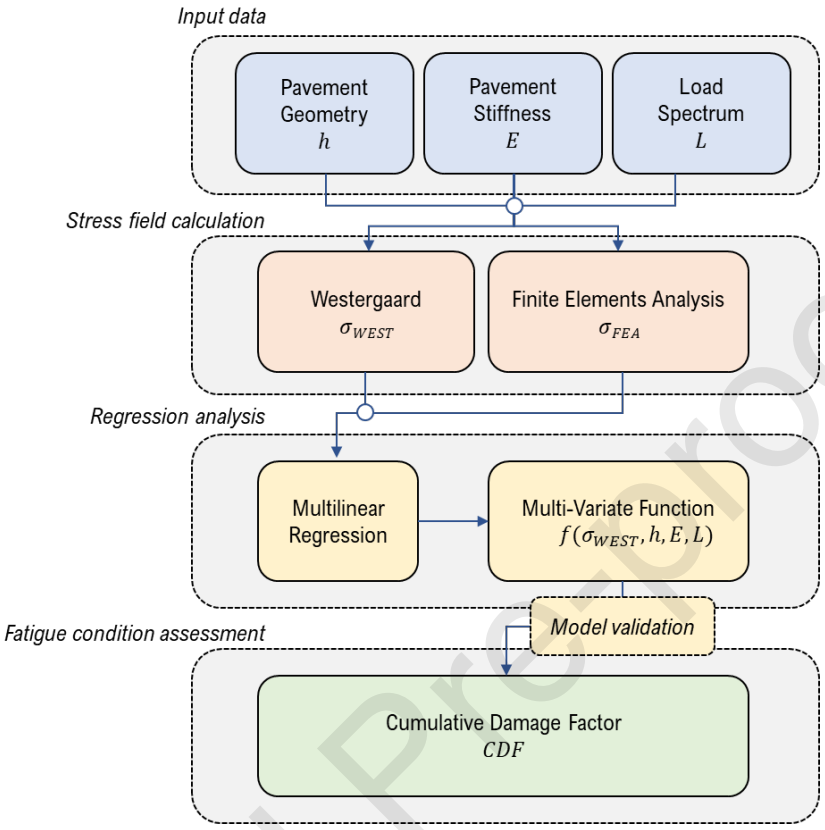

Figure 1: Scheme of the proposed methodology

- Mechanical layout, identifying for each airplane landing gears longitudinal and transversal configuration (e.g., single, tandem or tridem axles carrying single or dual wheels), maximum take-off weight ($MTOW$), tire inflation pressure, center of gravity location, load distribution between main and nose landing gears (GW). By reconstructing the physical scheme of forces governing the aircraft undercarriage, the weight (P) exerted by each gear leg and, ultimately, single wheel is determined.
- Geometrical footprints, concerning the static interaction of aircraft weighing tires with airport pavement. Dividing the single wheel load by the tire inflation pressure, the tire contact area is evaluated and the correspondent tire contact width (T_w) and length (T_l) are estimated (36). To account for the load superimposition, it is recommended to

consider longitudinal axles (e.g., single, tandem, tridem) and transverse wheel spacing (e.g., single, dual, trial) (S, S_T), as illustrated in Figure 2.

- Traffic composition, quantifying the actual load repetitions of the stress applied over the expected service life. It is common practice in pavement engineering to consider as passages only the aircraft ground operations at $MTOW$ [37]. Due to the varying aircraft wander, gear configuration and load magnitude, the number of aircraft passes is not sufficient to describe the number of load coverages, namely, the repetitions of maximum tensile stresses occurring at a specific point. To this intent, the pass–to–coverage (P/C) ratio has been introduced as the inverse of the probability that the effective tire contact patch of a passage covers a given pavement strip ([37]; [38]).

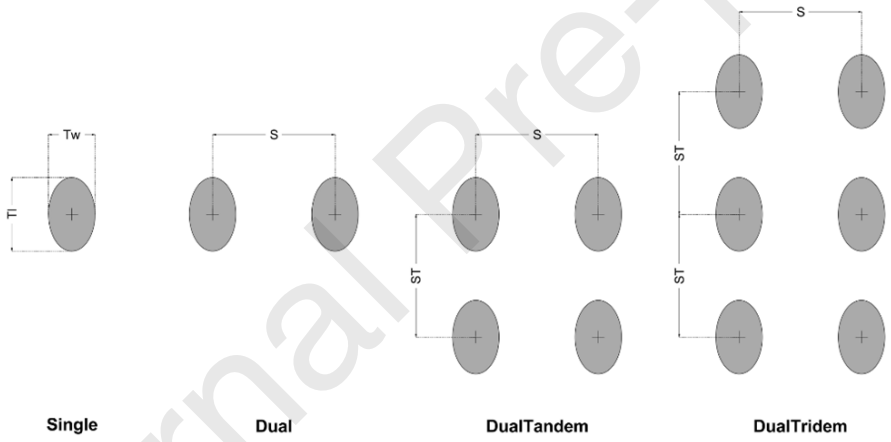

Figure 2: Layout of wheel arrangements and geometrical footprints [33]

In order to generate a sufficient number of load simulations for the multivariate analysis, a consistent data set of landing gear configurations with varying geometric and load features ([29]; [31]) is created. The characteristics of the aircrafts included in the set are reported in Table 3. Specifically, both theoretical and commercial loads are considered in order to test the methodology on the most heterogeneous dataset possible.

Aircraft	**Gear**	$MTOW$ **(kN)**	**Tire Press. (MPa)**	GW **(%)**	T_w **(m)**	T_l **(m)**	S **(m)**	S_T **(m)**
Single Whl-5	S	22.25	0.33	95	0.159	-	-	-
Single Whl-20	S	89.00	0.52	95	0.260	-	-	-
Single Whl-75	S	333.73	0.83	95	0.390	-	-	-
Citation 550 B	S	66.75	0.896	95	0.168	-	-	-
DC 3	S	112.14	0.310	95	0.370	-	-	-
Conquest II	S	44.16	0.655	95	0.160	-	-	-
Dual Whl-15	D	66.75	0.40	95	0.183	-	0.279	-
Dual Whl-50	D	222.49	0.55	95	0.277	-	0.508	-
Dual Whl-200	D	889.94	1.379	95	0.350	-	0.863	-
A 320-200 St	D	724.96	1.379	95	0.316	-	0.927	-
B 737-100	D	493.92	1.082	95	0.294	-	0.775	-
B 737-900 ER	D	837.44	1.517	95	0.324	-	0.864	-
Dual Tan-100	2D	444.97	0.827	95	0.226	0.361	0.508	1.143
Dual Tan-200	2D	889.94	1.103	95	0.277	0.443	0.533	1.168
Dual Tan-400	2D	1779.90	1.378	95	0.350	0.560	0.762	1.397
B 757-300	2D	1205.85	1.344	95	0.292	0.467	0.863	1.143
A 330-300 St	2D	2265.13	1.420	95	0.389	0.623	1.397	1.981
A 340-600 St	2D	3739.56	1.613	72	0.408	0.653	1.397	1.981
Dual Tri-100	3D	667.46	0.827	95	0.226	0.361	0.508	1.143
Dual Tri-300	3D	1334.93	1.103	95	0.277	0.443	0.533	1.168
Dual Tri-600	3D	2669.84	1.379	95	0.429	0.686	0.762	1.397
B 777-200 ER	3D	2927.89	1.413	95	0.362	0.579	1.397	1.448
B 777-300	3D	2945.75	1.480	95	0.355	0.567	1.397	1.448
A 380-800 Belly	3D	5513.22	1.503	57	0.373	0.597	1.529	1.699

Table 3: Library of landing gear mechanical and geometrical configurations.

3.2. Pavement Configuration

A concrete pavement is generally articulated in bearing, intermediate and subgrade layers, each designed with mechanically characterized constitutive materials and precise geometrical dimensions. Based on design loads and function, each layer is therefore associated with a specific strain - stress behavior given by elastic modulus (E), Poisson coefficient (ν), and concrete flexural strength (R). However, careful survey and constant monitoring activities are required to assess pavement state decay over time, as the design parameters are likely not to match the actual construction, loading and environmental conditions. Ultimately residual bearing residual capacity and superficial operability of each elementary unit are to be determined by investigating the following properties:

- Geometrical layer configuration, layers thickness and three-dimensional superstructure configuration through Ground Penetrating Radar (GPR). GPR studies the interaction of electromagnetic waves with dielectric properties of rigid pavement materials to detect layer thickness and material interfaces, as illustrated in Figure 3.

- Mechanical elastic capacity, global pavement elastic response and elastic modulus of the superstructural layers through the Heavy Weight Deflectometer (HWD). HWD measures the acoustic deflective basin of the pavement caused by impulsive fall of standardized weight. Through a back–calculation of captured wave response based on layer thicknesses GPR layout, elastic modules of each layer are iteratively assessed.

Figure 3: Layout and layers of a generic rigid pavement unit

Assuming standard slab dimensions and concrete elastic modulus, concrete thickness, and subgrade stiffness are the main variables driving different mechanical responses ([32]; [39]; [40]), specifically investigated through the main superstructural configurations reported in Table 4.

Layer	**Material** (41)	**Thickness (mm)**	**Size (m)**	E **(MPa)**	ν **(-)**
Surface P-501	Cement Concrete	300/350/400	5×5	27579	0.15
Sub-base P-209	Crushed Aggregates	300	-	278	0.35
Subgrade	Natural Soil	-	-	50/100/150	0.4

Table 4: Dataset of main rigid pavement geometrical and mechanical features

4. Stress field calculation

The static application of traffic loads induces bending tensile stresses at the bottom of the concrete layer. Rarely surpassing instantaneous concrete flexural strength, the impact of repetitions of tensile stresses induced by air traffic mix is verified against fatigue residual life of geometrically and mechanically characterized superstructures. A rigid pavement stress field due

to mechanical loads is generally evaluated separately through rational models, i.e., discrete analytical closed – form solutions or finite element analysis (FEA).

4.1. Theoretical framework

Closed – form solutions were first developed by Westergaard ([8]; [9]), adapting Kirchoff's plate theory to the simplified case of large concrete slabs resting on liquid foundations for single wheel circular application at the corner (Eq. 1), interior (Eq. 2) and edge (Eq. 3) of the slab:

$$\sigma_c = \frac{3P}{h^2}\left[1 - \left(\frac{a\sqrt{2}}{l}\right)^{0.6}\right] \tag{1}$$

$$\sigma_i = \frac{3(1+\nu)P}{2\pi h^2}\left(\ln\frac{l}{b} + 0.6159\right) \tag{2}$$

$$\sigma_e = \frac{3(1+\nu)P}{\pi(3+\nu)h^2}\left(\ln\frac{Eh^3}{100ka^4} + 1.84 - \frac{4\nu}{3} + \frac{1-\nu}{2} + \frac{1.18(1+2\nu)a}{l}\right) \tag{3}$$

Where P (N) is the wheel load transferred by the gear; E (MPa), ν (-) and h (mm) are respectively the elastic module, Poisson coefficient and thickness of the concrete slab; k (N/mm^3) is the subgrade reaction module (42); a (mm) and b (mm) are the effective radius and the thickness-dependent radius of the load footprint, respectively; l (mm) is the radius of relative stiffness.

Traditionally, P is defined by considering an equivalent single wheel load (ESWL) [10] to account for multi-wheel load interactions. However, such an equivalence heavily affects the ultimate accuracy of the stress model, as demonstrated by Caliendo and Parisi [43] and Mathi and Nallasivam [40]. In addition, the determination of ESWL depends on empirical corrective factors or chart-based procedures ([44]; [45]), which hardly comply with the rapid and automatic methodology pursued in this study.

4.2. Finite Element Analysis

The implementation of FEA software based on finite 2-D plate ([10]; [27]) and 3-D brick elements ([28]; [29]) approaches ultimately broadens the capability of traditional stress field calculation. In fact, more realistic hypothesis

of solid or layered foundations, subgrade elastic modulus, layer contact, and friction interaction, slab finite horizontal dimensions, joints contribution can be studied. Despite being widely acknowledged as accurate, FEM techniques are found to be computationally onerous and hardly customizable by non-field-related experts. As a result, they are typically run through closed software at the aggregate scale of sample units at the expense of surveys level of detail.

4.3. Comparative analysis

To pursue a valid mechanical model viable in the proposed monitoring and management framework, analytical models are investigated and compared to existing FEA procedures. To this end, a subset of typological and commercial aircraft landing gear and common pavement properties, respectively reported in Table 3 and Table 4, has been considered. The comparative theoretical and numerical calculation of static stress fields induced by one passage of each aircraft gear in various pavement configurations assesses the degree of viability of Westergaard closed-form solutions. In particular, the relevant numerical FEA solutions run on well-known commercial software (i.e., FEAFAA, [29]) have been used as reference.
The comparison between Westergaard's and FEA methods is, among the other, useful in highlighting the influence of pavement variables (slab thickness and subgrade elastic module ([40], [43])) and aircraft gear (single wheel, dual wheels, dual tandem, dual tridem) on both mechanical behavior of the slab and agreement between the two methods, as examined in Figures 4 and 5.

In fact, both subgrade stiffness and slab thickness variables are considered into Eqs. 1-3 through h, E_{sub}, k, l and b parameters. However, their impact on the final stress value is verified under the strict hypothesis of a single application load, which does not comply with all gears in Table 3 rather than single gears. In addition, Westergaard's equations neglect the contribution of intermediate layers on the stress field response by assuming a liquid foundation, which hardly complies with the typical multi-layered configuration considered for simulations. Therefore, a mismatch between theoretical and numerical results is expected to vary along with the subgrade stiffness E_{sub} and slab thickness h, especially for complex gears.

Indeed, a decay in E_{sub} (right to left in Figure 4) seems to limit the reliability of Westergaard's finite solutions, exacerbating dispersion and mean

error against FEA outputs. This is most likely due to the different layer interaction modeling due to the presence of an intermediate layer in FEA simulations, which is not taken into account in Westergaard's and that is most impacting for lower values of E_{sub}.

Conversely, a decrease in h (bottom to top in Figure 4) heavily influences concrete absolute tensions, with the maximum stress range moving from 3-4 MPa to 6-7 MPa, approximately, but only slightly affecting mean error and dispersion around performed simulations. This is to be expected, since the influence of slab thickness is modeled in both the theoretical and numerical models, thereby limiting the differences to those caused by superimposition effects.

In general, a proportional increment in E_{sub} and concrete slab thickness (up-left to down-right diagonal in Figure 4) leads to a uniform decrease in absolute value and relative error of discrete solutions.

To explicit the contribution of gear configuration and load condition, Figure 5 distinguishes the simulations in interior and edge loads per wheel arrangement. Single wheel applications - as by assumption in Westergaard's theoretical formulation - feature a close correlation between discrete and numerical solutions. In more complex gears, the same theoretical hypothesis evidently underestimates superimposition effects due to parallel and consecutive wheels. In fact, a distinctive relative mean error from FEA outputs is to be expected due to dual wheels load transversal stress profiles' interaction. Accordingly, further addition of longitudinal axles, tandem and especially tridem, results in an evident overall dispersion and slight decrease in finite–solution mean error. The distinction in interior and edge load shows a closer agreement between edge models, with central loading consistently misestimating FEA outputs with approximately same dispersion, but inferior mean error. Clearly, edge conditions tend to be more critical than interior ones in terms of maximum tensions induced at the base of rigid pavement's concrete slab.

Figure 6 synthesizes the results shown in Figures 4 and 5 in terms of Relative Mean Error (RME) between σ_{West} and σ_{FEA} for each load and pavement configuration. Westergaard's average limited applicability to complex gear arrangements is evident especially in interior load cases, with RME values progressively increasing as dual tandem and dual tridem gears are considered

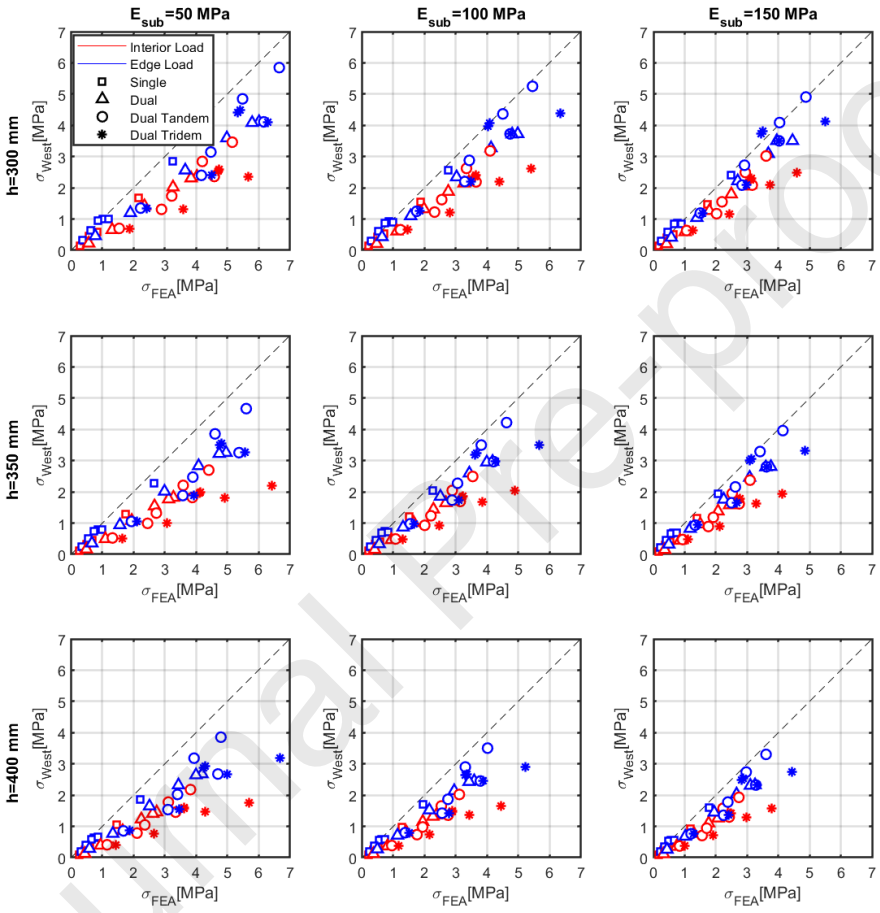

Figure 4: Scatter plot of Edge and Internal bottom tensile stress calculated numerically (σ_{FEA}) and analytically (σ_{West}) for different pavement configurations

(i.e., left to right in Figure 6).

5. Regression Analysis

5.1. Regression set up

As observed in Section 4.3, despite loading positions and pavement characteristics are being directly addressed in Westergaard's closed - form solutions, the latter lacks in consistently assessing tensile stresses, especially in multiple wheel configurations. To compensate such limits and raise the general reliability of the analytical solution, a multi-linear regression is performed. In particular, in both load conditions considered, Westergaard's bending tensile stress σ_{West} is being adopted as independent variable (directly driven by the slab's thickness and subgrade's elastic module) with the longitudinal and transverse wheel spacing properties selected as independent variables. Therefore, the following coefficients are being deployed in previous closed-form solutions: a coefficient addresses the compensation of Westergaard's simplifying assumptions (e.g., intermediate layer neglect); b and c coefficients account for the superimposition effects due to, respectively, longitudinal and transverse gear configuration. Accordingly, the equation of the resulting prediction model is the following:

$$\sigma_{PRED} = a \cdot \sigma_{West} + b \cdot S^* + c \cdot S_T^* \tag{4}$$

Where S^* and S_T^* are the net wheel spacings obtained by subtracting the wheel dimensions T_w and T_l to S ad S_T, respectively. The relevant parameters for each considered gear are reported in Table 3.

5.2. Regression outcomes

The results of the regression are reported in Table 5, listing model coefficients and statistical performance parameters for all considered gears in both edge and internal load conditions. In addition, Table 6 reports the significance analysis parameters of the multivariate model. For all gears and load conditions, the multivariate model is found to be statistically robust, as indicated by *F Stat* values. Lastly, the *p values* show all the variables to be significant, with the only exception of b coefficient for dual gears in edge loadings.

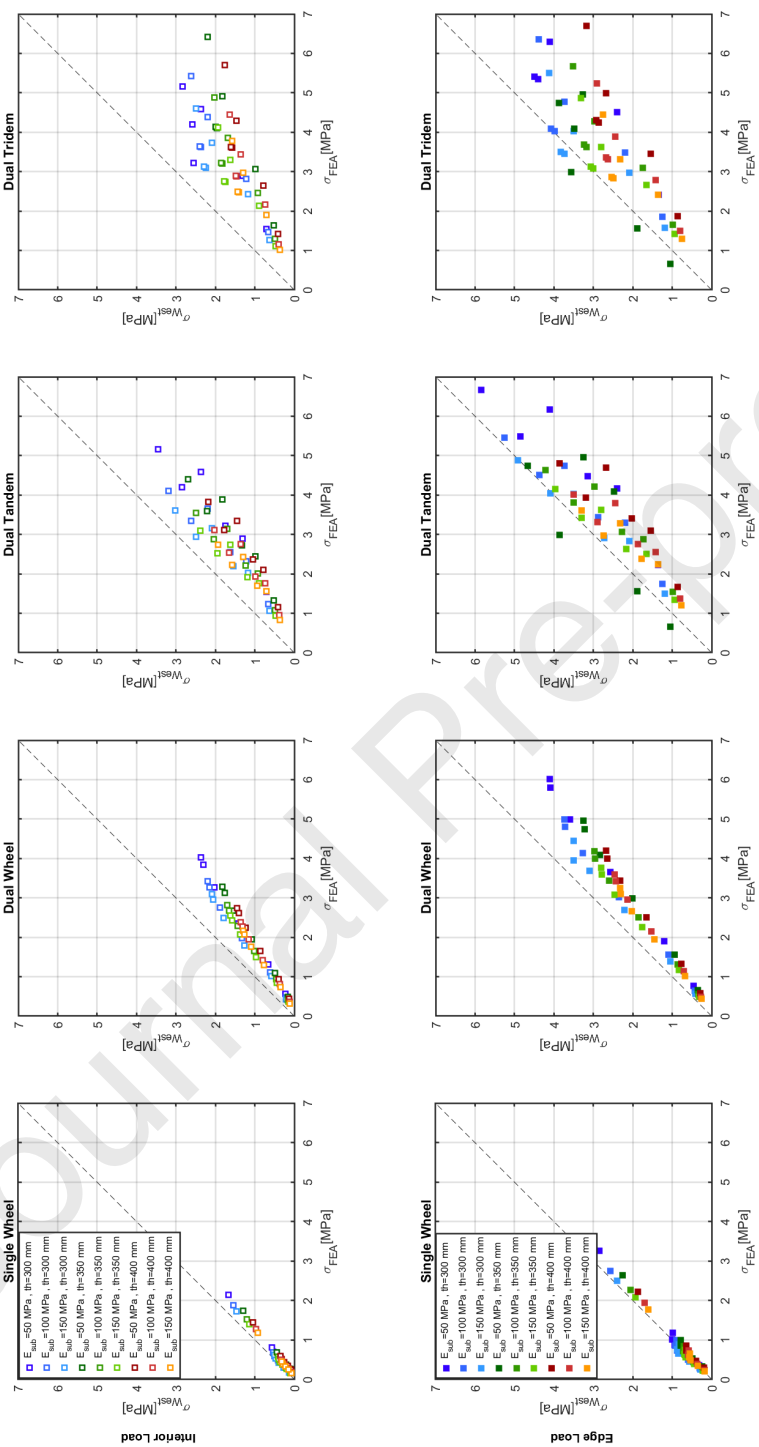

Figure 5: Scatter plot of Edge and Internal bottom tensile stress calculated numerically (σ_{FEA}) and analytically (σ_{West}) for different wheel arrangements

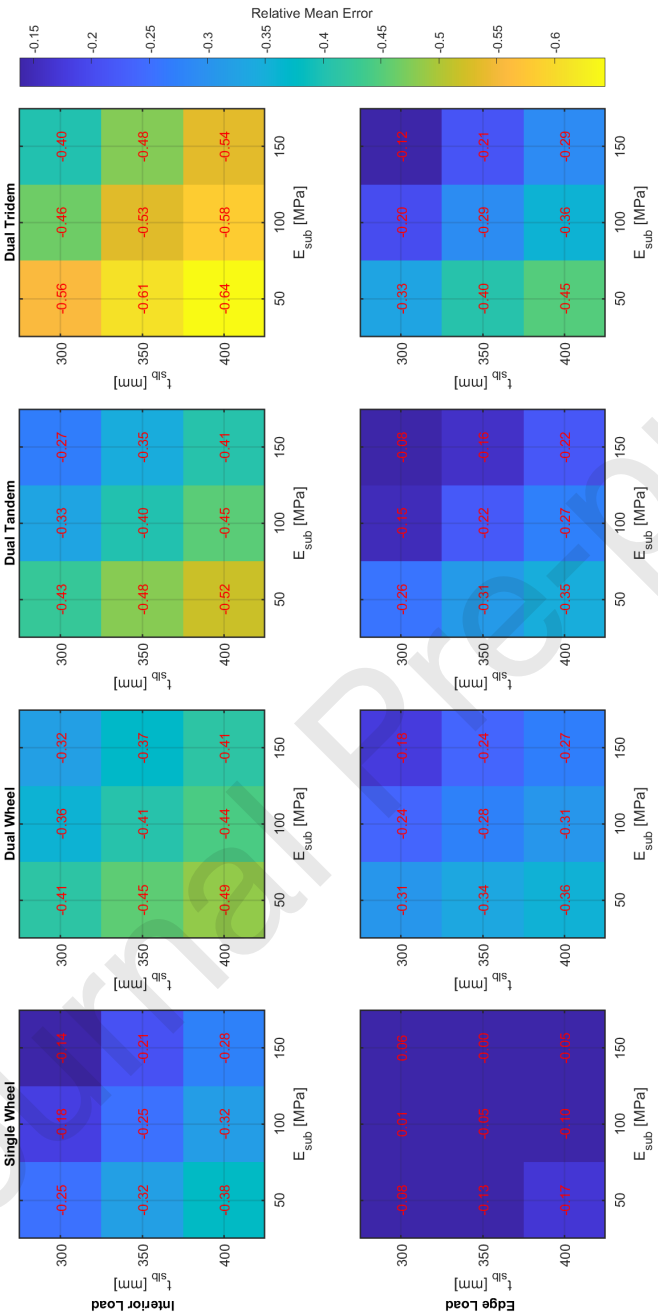

Figure 6: Relative Mean Error (RME) between discrete and numerical simulations at varying thickness and stiffness, calculated for different load condition (rows) and gear configuration (columns).

Gear	**Load**	a	b	c	**Mult. R**	$\mathbf{R^2}$	**Std Err.**	**95% conf. interval**	**75% conf. interval—**
S	int.	1.29	-	-	0.99	0.99	0.07	-0.10/0.16	-0.05/0.10
S	edge	1.06	-	-	0.99	0.99	0.10	-0.22/0.18	-0.14/0.10
D	int.	1.49	0.44	-	0.97	0.95	0.20	-0.32/0.40	-0.17/0.24
D	edge	1.36	0.07	-	0.98	0.97	0.24	-0.46/0.52	-0.26/0.32
2D	int.	1.55	-1.32	1.01	0.89	0.78	0.44	-0.77/0.88	-0.43/0.54
2D	edge	1.34	-2.29	1.28	0.90	0.80	0.53	-0.92/1.04	-0.51/0.64
3D	int.	1.71	-0.94	1.51	0.85	0.74	0.63	-1.4/1.33	-0.83/0.76
3D	edge	1.15	-1.22	1.84	0.84	0.71	0.73	-1.62/1.54	-0.97/0.88

Table 5: Regression coefficients and predictive model descriptive statistics for different wheel arrangements and load conditions

Gear	**Load**	F-**Stat**	p	t_a-**Stat**	p	t_b-**Stat**	p	t_c-**Stat**	p
S	int.	6365.85	0.00	79.79	0.00	-	-	-	-
S	edge	6529.40	0.00	80.80	0.00	-	-	-	-
D	int.	3458.43	0.00	19.80	0.00	2.58	0.01	-	-
D	edge	4149.88	0.00	21.66	0.00	0.58	0.56	-	-
2D	int.	727.43	0.00	12.46	0.00	-4.59	0.00	5.08	0.00
2D	edge	937.87	0.00	14.70	0.00	-5.96	0.00	4.99	0.00
3D	int.	448.60	0.00	9.38	0.00	-2.15	0.04	3.82	0.00
3D	edge	446.97	0.00	8.70	0.00	-2.15	0.00	3.71	0.00

Table 6: Significance statistics of predictive model for different wheel arrangements and load conditions

5.3. Model validation

By applying eq. (4) for all gears included in the validation set of Table 7, it is possible to appreciate a good reliability of the regressed model in accounting for different load applications. The relevant results are shown in Figure 7 and Figure 8, for both the edge and internal load application. In particular, Figure 7 is evidence of a limited dependence of the model accuracy on variations of E_{sub} and h. Especially for low-thickness and high subgrade moduli, predicted values appear to moderately overestimate those obtained from FEA. On the other hand, for high thickness and low subgrade stiffness, PRED model tends to slightly underestimate FEA outputs. For these reasons, the extreme pavement conditions (top-right and bottom-left in Figure 7) would require additional efforts in refining proposed physical model layer interactions.

This is also observed in Figure 8, which plots stress fields for all gear classes. Specifically, the figure shows a close agreement between σ_{PRED} and σ_{FEA} for single and dual gears, gradually losing precision for dual tandem and, especially, dual tridem gears. The residual dispersion is reasonably to be related to Westergaard's simple wheel-elastic pavement interaction theory, requiring more complex analysis to directly interpret multiple wheel influence. Quantitative details of the prediction performance are reported in Table 8, with R^2 ranging from around 0.95 for S and D gears to around 0.65 for 2D and 3D gears.

Aircraft	**Gear**	$MTOW$ **(kN)**	**Tire Press. (MPa)**	GW **(%)**	T_w **(m)**	T_l **(m)**	S **(m)**	S_T **(m)**
Single Whl-10	S	44.50	0.33	95	0.22	-	-	-
Single Whl-45	S	200.24	0.62	95	0.35	-	-	-
Beechjet 400A	S	72.54	0.62	95	0.21	-	-	-
Shorts 360	S	121.04	0.54	95	0.29	-	-	-
Skyhawk 172	S	11.38	0.34	95	0.11	-	-	-
Dual Whl-30	D	133.49	1.03	95	0.16	-	0.31	-
Dual Whl-100	D	444.97	0.97	95	0.30	-	0.58	-
A 318-100 St	D	553.28	1.02	95	0.32	-	0.93	-
A 321-200 Opt	D	921.16	1.50	95	0.34	-	0.93	-
B 737-500	D	596.26	1.34	95	0.29	-	0.77	-
Dual Tan-150	2D	667.46	0.97	95	0.26	0.41	0.51	1.14
Dual Tan-300	2D	1334.93	1.24	95	0.32	0.51	0.66	1.30
B 747-400 Belly	2D	3902.43	1.38	47	0.36	0.59	1.14	1.47
B 767-400 ER	2D	2006.83	1.48	95	0.36	0.57	1.16	1.37
A 340-300 St	2D	2706.58	1.42	85	0.40	0.64	1.40	1.98
Dual Tri-225	3D	1001.19	0.97	95	0.26	0.41	0.51	1.14
Dual Tri-450	3D	2002.38	1.24	95	0.32	0.51	0.66	1.30
B 777-200	3D	2434.06	1.25	95	0.35	0.56	1.40	1.45
B 777-200 LR	3D	3417.39	1.50	95	0.37	0.61	1.40	1.46
B 777-300 ER	3D	3457.45	1.52	95	0.38	0.61	1.40	1.46

Table 7: Library of landing gear mechanical and geometrical configurations used for validation purposes

Gear	Load	R^2	Std Err.	95% conf. interval	75% conf. interval—
S	int.	0.95	0.07	-0.10/0.15	-0.05/0.1
S	edge	0.96	0.09	-0.20/0.12	-0.14/0.05
D	int.	0.93	0.22	-0.37/0.46	-0.19/0.29
D	edge	0.97	0.23	-0.41/0.47	-0.23/0.28
2D	int.	0.63	0.49	-0.68/1.07	-0.32/0.71
2D	edge	0.67	0.58	-0.81/1.26	-0.38/0.83
3D	int.	0.65	0.59	-1.27/0.74	-0.86/0.32
3D	edge	0.60	0.68	-1.48/0.90	-0.98/0.41

Table 8: Validation of predictive model descriptive statistics for different wheel arrangements and load conditions

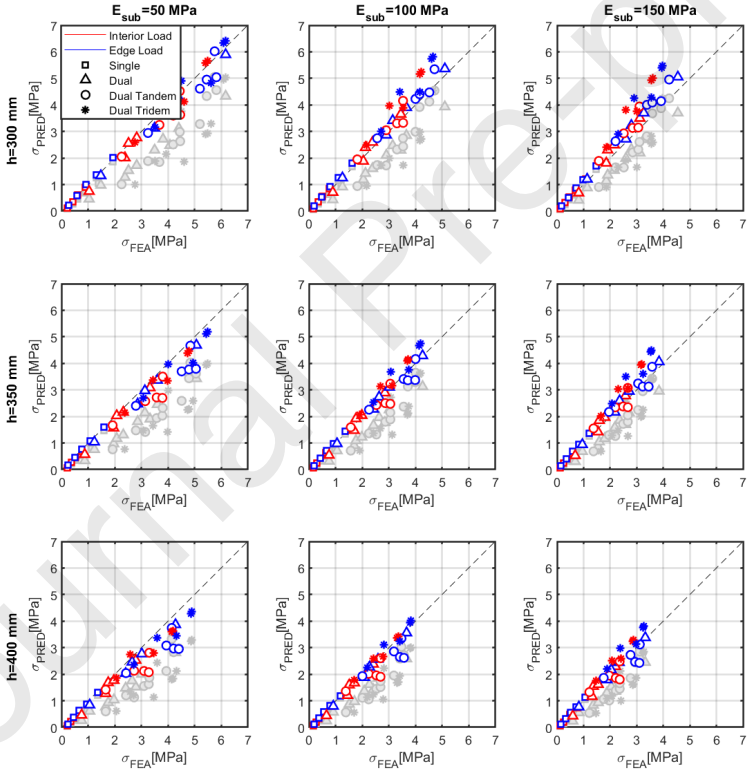

Figure 7: Scatter plot of tensile stress calculated numerically (σ_{FEA}) and predicted by model (σ_{PRED}) for different pavement configurations. Comparison between (σ_{FEA}) and (σ_{West}) is plotted in gray.

6. Fatigue Condition Assessment

6.1. Background

The good agreement of the prediction model with FEA results in Section 5 drives the calculation of the concrete slab CDF. By applying the concrete slab fatigue empirical failure criterion by FAA [30], the number of critical coverages $C_{e,i}$ of horizontal tension σ_i exerted by a generic i^{th} aircraft empirically depends on pavement response behavior and load condition:

$$C_{e,i} = 10^{\left\{\frac{R}{\sigma_i} - \left[\frac{(1-SCI/100)(ad-bc)+bc}{(1-SCI/100)(d-b)+b}\right]\right\} / \left[\frac{bd}{(1-SCI/100)(d-b)+b}\right]} \tag{5}$$

Where $SCI(-)$ is the Structural Condition Index accounting for specific rigid pavement distresses [29]; a, b, c are non-dimensional empirical calibration parameters related to the pavement layering [30]; σ_i (MPa) is the maximum bending tensile stress at the bottom of the concrete slab due to the i^{th} static load [29].

Therefore, the elementary damage $D_{e,i}$ potentially sustainable by the considered pavement due to one i^{th} aircraft coverage is equal to the inverse of the same aircraft critical coverages $C_{e,i}$. The total longitudinal damage $D_i^{x_j}(y)$ caused by a longitudinal horizontal stress profile $\sigma_i(x_j, y)$ of a single i^{th} aircraft coverage at each j^{th} transversal distance x_j from centerline is then calculated as graphically visualised in Figure 9 and expressed in Equations 6.1-6.1.[33]

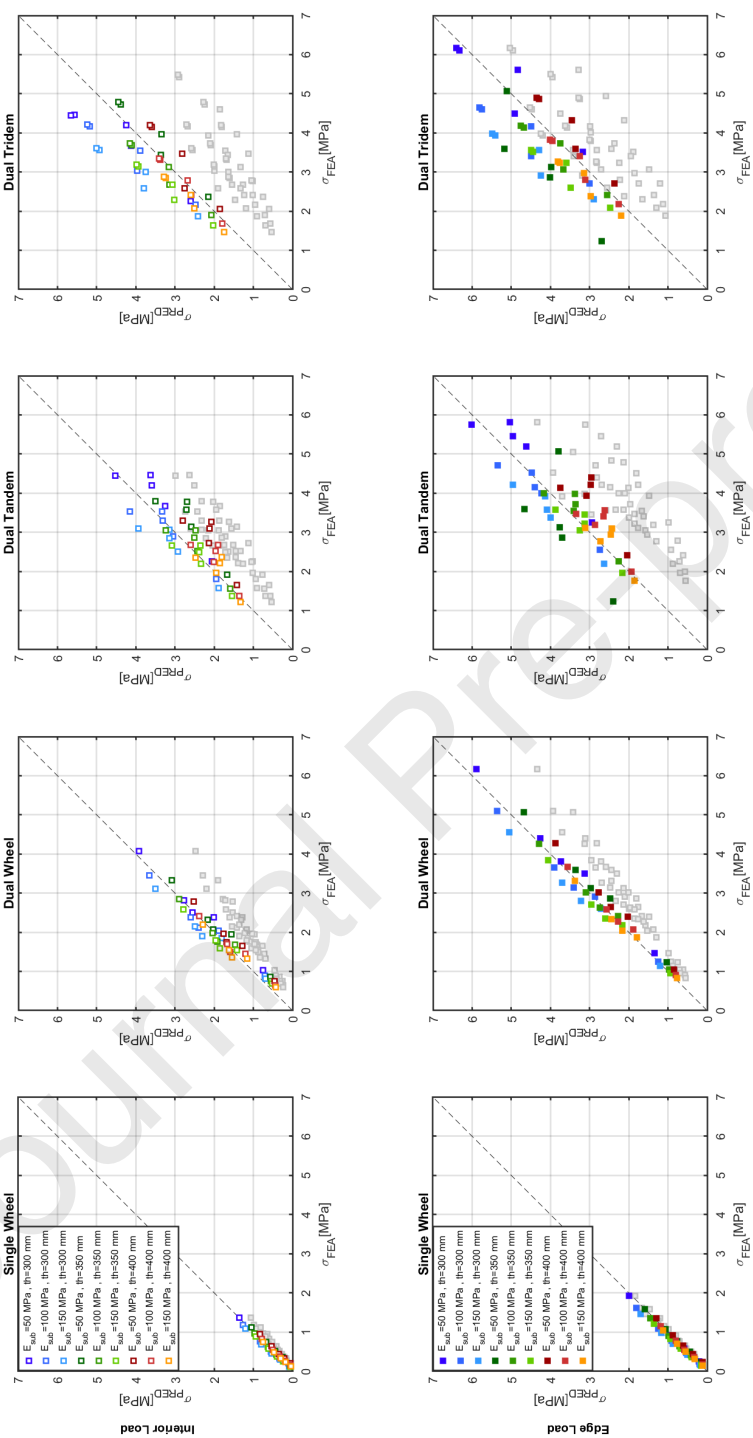

Figure 8: Scatter plot of Edge and Internal bottom tensile stress calculated numerically (σ_{FEA}) and predicted by the multivariate analysis (σ_{PRED}) for different wheel arrangements. The comparison between (σ_{FEA}) and (σ_{West}) is plotted in gray.

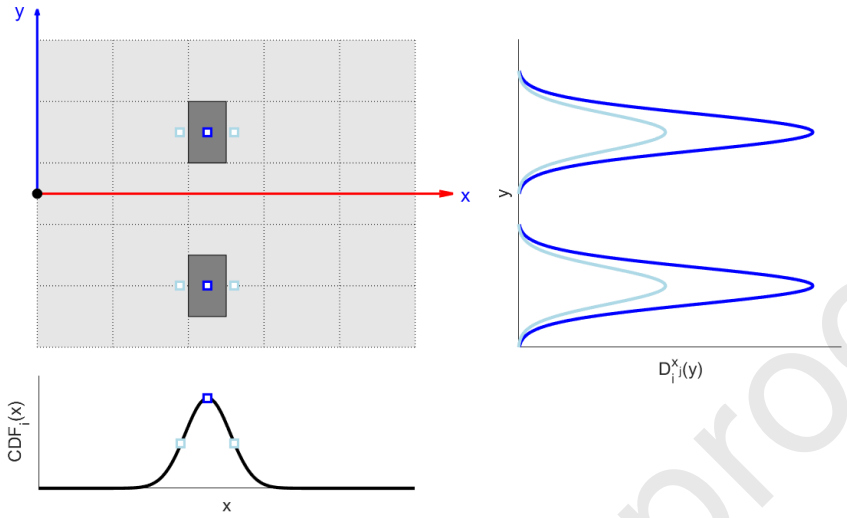

Figure 9: Longitudinal damage profile $D_i^{x_j}(y)$ and $CDF_i(x)$ profile due to a generic single tandem gear (2S) load

$$D_i^{x_j}(y) = \frac{1}{P/C_{i,x_j}} \int_{y=-\infty}^{y=+\infty} \frac{d\left(D_{e,i}\left(x_j, y\right)\right)}{d\sigma_i\left(x_j, y\right)} \frac{d\sigma_i(x_j, y)}{dy}\ \theta(\sigma_i)\ dy \tag{6}$$

where

$$D_{e,i} = \frac{1}{C_{e,i}} \tag{7}$$

$$\theta(\sigma_i) = \begin{cases} 0 & \text{if } \sigma_i \leq 0, \\ \sigma_i & \text{if } \sigma_i > 0. \end{cases} \tag{8}$$

The cumulative sum of each longitudinal total damage $D_i^{x_j}(y)$ per transverse distance x_j represents the total transverse damage profile $D_i(x)$ of a single i^{th} gear coverage. Accordingly, the total cumulative damage $CDF_i(x)$ of each aircraft can be determined with Miner's law, accounting for expected passages N_i of generic aircraft over hypothesized service life.

$$CDF_i(x) = D_i(x)N_i \tag{9}$$

The sum of each aircraft CDF_i profile results in the total cumulative damage factor profile CDF of a specific pavement section due to air traffic mix .

6.2. CDF calculation

The CDF calculation method must be applied to the proposed predictive model and tested against numerical evidence. In particular, FEA provides inherent tensile profiles ($\sigma_{FEA}(x, y)$) as inputs for total longitudinal damage $D_i^{x_j}(y)$ calculation per x_j transversal distance. On the other hand, the output of proposed stress prediction model only assesses the maximum bending tension (σ_{PRED}) at the bottom of concrete slab. Assigned a normal wheel coverage probability of maximum tension at each transverse distance from the centerline due to low lateral wandering (33), an equivalent cumulative maximum damage profile CDF_{PRED} is calculated per single or multiple maximum tensile peaks. To discern the degree of discrepancy between CDF_{FEA} and CDF_{PRED} models, the maximum values of FEA stress distributions (σ_{FEA}) are conveyed into a CDF_{FEA} profile by adapting the previous normal wheel probability function.

Having set an intermediate pavement configuration ($E_{sub} = 100MPa$, $h = 350mm$) and assumed a reference aircraft for each gear arrangement studied (see Figure 10), the proposed cumulative damage factor $CDF_{i,PRED}$ model fed by regressed $\sigma_{i,PRED}$ is compared with numerical $CDF_{i,FEA}$ profile in Figure 10.

For the considered subset of aircraft, σ) values are calculated through both approaches for edge and interior load cases. The most sever stress conditions are selected to drive the CDF evaluation. For instance, the dual tridem presented in Figure 10 is critical to interior loading and requires an evident dual peak approximation due to bimodal stress distribution with two equivalent maximum peaks. The other cases - where edge loading prevails - are not affected by the same multi-peak approximation. As an instance, the dual tandem CDF curve reported in Figure 10 shows a dual-peak tensile behavior, with one absolute and one relative maximum. Consequently, the 2D cumulative damage configuration is built on a single absolute maximum stress value, closely fitting FEA results. The proposed approximation closely matches numerical outputs, underlining ultimate effectiveness of the proposed CDF calculation method.

Summarizing, even with longitudinal damage profile simplifications, Figure 10 is evidence of a good agreement between proposed and numerical CDF_i model, despite the residual stress dispersion intrinsic to dual tridem and tandem gear configurations. In fact, the $CDF_{i,PRED}$ and $CDF_{i,FEA}$ of selected gear arrangements are relatively close in terms of absolute value, with the maximum relative difference being strictly dependent on the specific gear and ranging, for the considered subset of aircraft, between $\pm 25\%$.

7. Conclusions and future discussions

The paper studies a rapid and direct stress field and fatigue assessment procedure in airport rigid pavement management systems. First, state-of-the-art issues in monitoring and maintaining concrete pavements are explained through an overview on APMS applications and input data in terms of surveyed pavement and load conditions. Stressing the need for a reliable proactive stress and damage protocol updatable with every monitoring routine and sustainable under the computational demand as a step forward with respect to the current approaches.
In fact, the state-of-the-art procedures are either based on very accurate finite element models, highly demanding in terms of modeling expertise and computational resources, or rapid closed-form analytical solutions, which evidently suffer in accuracy due to the simplification assumptions. Accordingly, a multivariate regressive analysis is performed to compensate limits of existing analytical closed-form solutions while allowing for rapid application. Results obtained on various simulation scenarios with the proposed method are compared to same simulations run on FEA environment. A brief summary of outcomes is here listed:

- Subgrade's stiffness and concrete slab's thickness are investigated as superstructural independent variables, sensibly raising the general coherence of proposed model with monitored pavement parameters. Extreme values are found to affect, even if slightly, the reliability of the proposed stress prediciton model. To extend the latter's general feasibility, additional efforts should be paid in simulating also slab horizontal dimensions, intermediate layer and load transfer joint mechanical contributions. A statistical validation on pavement varying structural inputs (e.g., intermediate layers thickness and material) should be further performed, to explicitly extend the range of applicability of the proposed model.

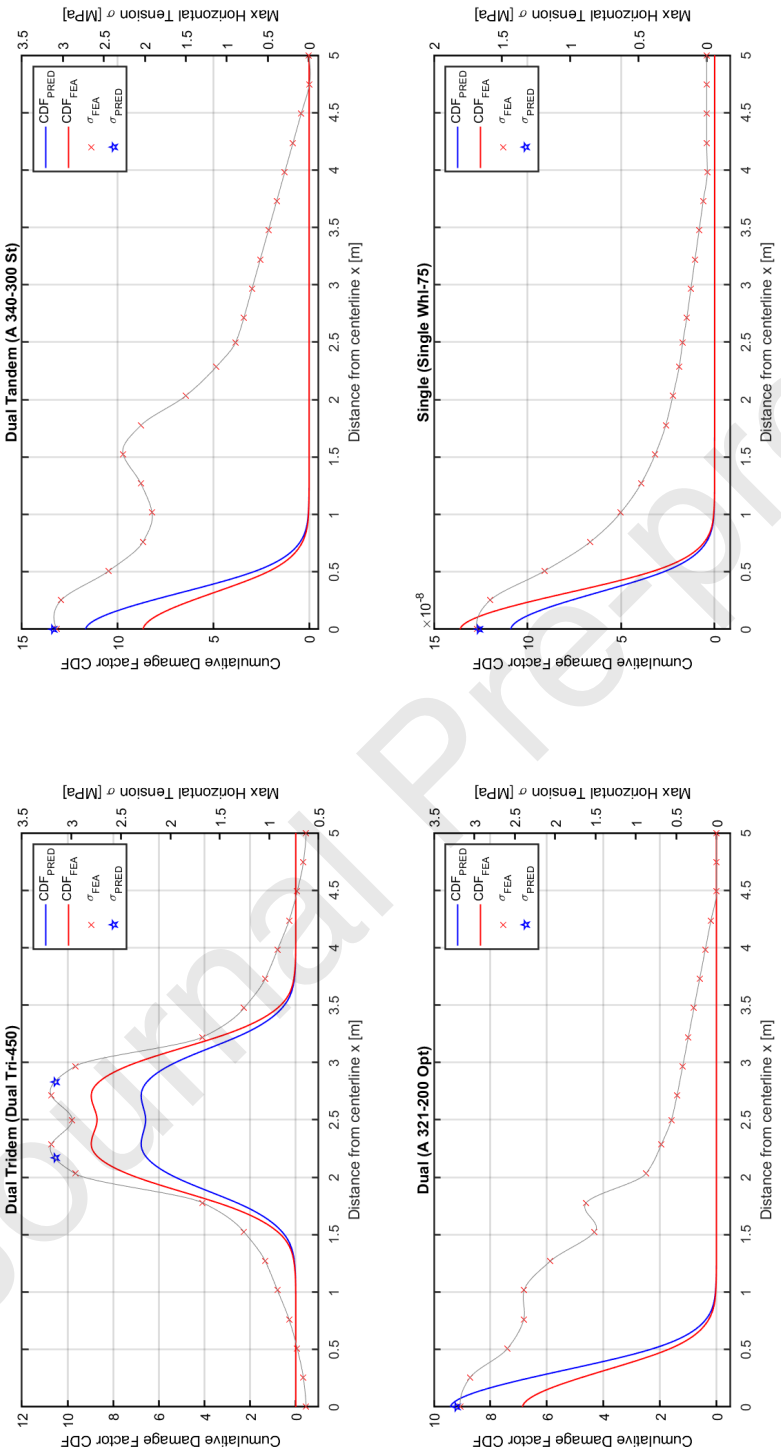

Figure 10: Comparison of CDF profiles calculated through FEA and Pred models over an intermediate pavement configuration due to the reference aircraft gear arrangement

- A strong correlation has been observed for all the different gear arrangements. Specifically, single and dual wheel configurations closely match numerical results, while dual tandem and dual tridem still exhibit a good reliability despite a non-negligible residual dispersion. This residual discrepancy derives from Westergaard's simplified elastic plate theory reliant on one wheel load configuration. Therefore the non-linear influence of multiple wheel loads has been addressed through two correspondent independent regressive parameters. Considering numerical outputs as reference for the proposed predictive model, more advanced analytical solutions should be further investigated to directly account for multiple wheel longitudinal and transverse interactions, thereby increasing the precision of the regressive analysis.

To assess the decaying performance of rigid pavement units throughout the set period of service, a bottom - up cumulative damage factor based on wheel coverage normal probability function is introduced and tested against FEA evidence. Particularly:

- Critical coverages, elementary damage and total maximum longitudinal damage are directly predicted per aircraft and pavement configuration. It is worthwhile mentioning that FEA longitudinal stress profiles provide a full survey of total longitudinal damage along n transverse distances or integration nodes per superstructural unit. Conversely, the proposed rapid model directly determines maximum total damage independently of the direction, thereby struggling in further analysing damage effects from tandem and tridem. While approximately sharing comparable absolute values of total cumulative damage via $CDF_{i,PRED}$ and via $CDF_{i,FEA}$, further studies need to be analytically or numerically performed to refine existing difference in CDF dispersion between predicted and finite element analysis.

- Total transverse cumulative damage factors are extracted from numerical longitudinal stress and damage profiles. Parallelly, regressive model's output maximum tensile stress and subsequent cumulative damage factor approximate CDF behavior of pavement and load condition with a wheel coverage probability normal distribution per absolute stress peaks. By assigning a low lateral wander, CDF_{PRED} matches CDF_{FEA} profile, ultimately resembling $\sigma_{i,FEA}$ distribution.

Future efforts should be conveyed into refining wheel coverage probability through a bi-dimensional or three-dimensional influence chart methodology.

The proposed methodology ultimately lays out a rapid and easily implementable survey data collection to CDF calculation protocol. To overcome the computational times demanded by a more accurate FEM model, the developed rapid solutions allow a directly interoperable stress and CDF calculation updatable with each survey routine. With a dataset layout of 20-30s, prediction computation time of 1-5s per elementary unit, the computational time saving is approximately 6 hours compared to FEA for a generic apron section of six sample units with 25 elementary units. Such a model, despite lacking in terms of maximum accuracy, still provides a robust prediction model potentially applicable to the entire rigid pavement asset. Being a regressed physics based model, the additional advantages are: easy understanding of CDF determining variables due to Westergaard's elastic theory formulation; and immediate implementation in a monitoring framework without the need for advanced computational resources or extended numerical expertise. The limits of present research encourage to pursue more physical-based model solutions, validated with numerical results, in order to raise the prediction accuracy and to forsee the management of an entire airport's rigid pavement asset through rapid assessments at the single slab scale.

References

[1] Federal Aviation Administration (FAA), Airport Pavement Management Program (PMP), 2023. [Online]. Available: `https://www.faa.gov/airports/resources/advisory_circulars`

[2] M. T. Miah, E. Oh, G. Chai, and P. Bell, An overview of the airport pavement management systems (APMS), *Int. J. Pavement Res. Technol.*, vol. 13, no. 6, pp. 581-590, Nov. 2020, doi: 10.1007/s42947-020-6011-8.

[3] Z. Liu, X. Gu, Q. Dong, S. Tu, and S. Li, 3D Visualization of Airport Pavement Quality Based on BIM and WebGL Integration, *J. Transp. Eng. Part B: Pavements*, vol. 147, no. 3, 2021, doi: 10.1061/JPEODX.0000280.

[4] P. di Mascio, A. Ragnoli, S. Portas, and M. Santoni, Monitor activity for the implementation of a pavement-management system at Cagliari airport, *Sustainability*, vol. 13, no. 17, Sep. 2021, doi: 10.3390/su13179837.

[5] G. White and S. Jamieson, Research Outcomes and Future Needs for Australian Rigid Airport Pavements, Apr. 2023.

[6] E. Heymsfield and J. S. Tingle, State of the practice in pavement structural design/analysis codes relevant to airfield pavement design, *Eng. Fail. Anal.*, vol. 105, pp. 12-24, Nov. 2019, doi: 10.1016/j.engfailanal.2019.06.029.

[7] J. Sun et al., A systematic review of structural design methods and nondestructive tests for airport pavements, *Constr. Build. Mater.*, vol. 411, Jan. 2024, doi: 10.1016/j.conbuildmat.2023.134543.

[8] H. M. Westergaard, Stresses in Concrete Pavements Computed by Theoretical Analysis, *Public Roads*, vol. 7, no. 2, pp. 25-35, Apr. 1926. [Online]. Available: `https://trid.trb.org/view/109814`

[9] H. M. Westergaard, New Formulas for Stresses in Concrete Pavements of Airfields, *Trans. Am. Soc. Civ. Eng.*, vol. 113, pp. 425-444, 1948. [Online]. Available: `https://ascelibrary.org/`

[10] Y. H. Huang, *Pavement Analysis and Design*, 2nd ed., vol. 1. Upper Saddle River, NJ: Pearson Prentice Hall, 2004. [Online]. Available: `https://www.pearson.com/en-us/subject-catalog/p/pavement-analysis-and-design/P200000003249/9780131424739`

[11] A. Elseicy, A. Alonso-Díaz, M. Solla, M. Rasol, and S. Santos-Assunçao, Combined Use of GPR and Other NDTs for Road Pavement Assessment: An Overview, *Remote Sens.*, vol. 14, no. 17, Sep. 2022, doi: 10.3390/rs14174336.

[12] V. Gagliardi et al., Satellite Remote Sensing and Non-Destructive Testing Methods for Transport Infrastructure Monitoring: Advances, Challenges and Perspectives, *Remote Sens.*, vol. 15, no. 2, Jan. 2023, doi: 10.3390/rs15020418.

[13] A. Joshaghani and D. G. Zollinger, Concrete pavements curing evaluation with non-destructive tests, *Constr. Build. Mater.*, vol. 154, pp. 1250-1262, 2017, doi: 10.1016/j.conbuildmat.2017.06.110.

[14] W. W. L. Lai, R. K. W. Chang, and J. F. C. Sham, A blind test of nondestructive underground void detection by ground penetrating radar (GPR), *J. Appl. Geophys.*, vol. 149, pp. 10-17, 2018, doi: 10.1016/j.jappgeo.2017.12.010.

[15] M. A. Rasol et al., GPR laboratory tests and numerical models to characterize cracks in cement concrete specimens, exemplifying damage in rigid pavement, *Measurement*, vol. 158, Jul. 2020, doi: 10.1016/j.measurement.2020.107662.

[16] A. Joshaghani and M. Shokrabadi, Ground penetrating radar (GPR) applications in concrete pavements, *Int. J. Pavement Eng.*, vol. 23, no. 13, pp. 4504-4531, 2022, doi: 10.1080/10298436.2021.1954182.

[17] A. M. Ioannides, Dimensional analysis in NDT rigid pavement evaluation, *J. Transp. Eng.*, vol. 116, no. 1, pp. 23-36, 1990, doi: 10.1061/(ASCE)0733-947X(1990)116:1(23).

[18] G. Fileccia Scimemi, T. Turetta, and C. Celauro, Backcalculation of airport pavement moduli and thickness using the Lévy Ant Colony Optimization Algorithm, *Constr. Build. Mater.*, vol. 119, pp. 288-295, 2016, doi: 10.1016/j.conbuildmat.2016.05.072.

[19] K. Gkyrtis, A. Loizos, and C. Plati, Integrating pavement sensing data for pavement condition evaluation, *Sensors*, vol. 21, no. 9, 2021, doi: 10.3390/s21093104.

[20] R. A. Tarefder and M. U. Ahmed, Consistency and accuracy of selected FWD backcalculation software for computing layer modulus of airport pavements, *Int. J. Geotech. Eng.*, vol. 7, no. 1, pp. 21-35, 2013, doi: 10.1179/1938636212Z.0000000009.

[21] M. Gao et al., InSAR time-series investigation of long-term ground displacement at Beijing Capital International Airport, China, *Tectonophysics*, vol. 691, pp. 271-281, Nov. 2016, doi: 10.1016/j.tecto.2016.10.016.

[22] L. Bianchini Ciampoli et al., Displacement monitoring in airport runways by persistent scatterers SAR interferometry, *Remote Sens.*, vol. 12, no. 21, pp. 1-14, Nov. 2020, doi: 10.3390/rs12213564.

[23] Y. Garini, I. T. Young, and G. McNamara, Spectral imaging: Principles and applications, *Cytometry A*, vol. 69A, no. 8, pp. 735-747, 2006, doi: 10.1002/cyto.a.20311.

[24] I. Garrido, S. Lagüela, and P. Arias, Infrared thermography's application to infrastructure inspections, *Infrastructures*, vol. 3, no. 3, Sep. 2018, doi: 10.3390/infrastructures3030035.

[25] E. Schnebele, B. F. Tanyu, G. Cervone, and N. Waters, Review of remote sensing methodologies for pavement management and assessment, *Eur. Transp. Res. Rev.*, vol. 7, no. 2, Jun. 2015, doi: 10.1007/s12544-015-0156-6.

[26] M. Soilán et al., Review of laser scanning technologies and their applications for road and railway infrastructure monitoring, *Infrastructures*, vol. 4, no. 4, Sep. 2019, doi: 10.3390/infrastructures4040058.

[27] A. M. Tabatabaie and E. J. Barenberg, Finite Element Analysis of Jointed or Cracked Concrete Pavements, *Transp. Res. Rec.*, vol. 671, pp. 11-19, 1978, doi: 10.3141/671-02.

[28] W. Davids, G. Turkiyyah, and J. Mahoney, EverFE: Rigid Pavement Three-Dimensional Finite Element Analysis Tool, *Transp. Res. Rec.*, vol. 1629, pp. 41-49, Apr. 1998, doi: 10.3141/1629-06.

[29] Federal Aviation Administration (FAA), Development of Advanced Computational Models for Airport Pavement Design, Washington, D.C., 1997. [Online]. Available: `https://www.tc.faa.gov/its/worldpac/techrpt/ar97-47.pdf`

[30] Federal Aviation Administration (FAA), Calibration of FAARFIELD Rigid Pavement Design Procedure, 2009. [Online]. Available: `https://www.tc.faa.gov/its/worldpac/techrpt/ar09-57.pdf`

[31] A. Rezaei Tarahomi et al., ANNFAA: artificial neural network-based tool for the analysis of Federal Aviation Administration's rigid pavement

systems, *Int. J. Pavement Eng.*, vol. 23, no. 2, pp. 400-413, 2022, doi: 10.1080/10298436.2020.1748627.

[32] A. Ioannides and J. P. Donnelly, Three-dimensional analysis of slab on stress-dependent foundation, pp. 72-84, Apr. 1988.

[33] International Civil Aviation Organization (ICAO), Aerodrome Design Manual - Part 3, 2023. [Online]. Available: `https://www.icao.int/publications/pages/publication.aspx?docnum=9157`

[34] Federal Airport Engineering Division AAS, 150/5335-5D, Standardized Method of Reporting Airport Pavement Strength - PCR, Apr. 2022 (updated Jan. 2025).

[35] R. Pinto, L. Bianchini Ciampoli, and A. Benedetto, Digital management of airport pavement: preliminary achievements on apron areas, *Transp. Res. Procedia*, In Press, 2024.

[36] A. T. Pereira, U. States, and W. E. S., Procedures for development of CBR design curves: final report, U. S. Engineer Waterways Experiment Station, Vicksburg, Miss., 1977. [Online]. Available: `https://catalog.hathitrust.org/Record/011420529`

[37] I. Kawa, Pass-to-Coverage Computation for Arbitrary Gear Configurations in the FAARFIELD Program, Dec. 2012.

[38] T. B. Pereira, On the Pass-to-Coverage Ratio, 2013. doi: 10.13140/RG.2.1.3919.5280.

[39] A. Ioannides, M. Thompson, and E. J. Barenberg, Westergaard solutions reconsidered, *Transp. Res. Rec.*, vol. 1043, pp. 13-23, Jan. 1985.

[40] K. K. Mathi and K. Nallasivam, Static analysis of rigid airfield pavement using finite element method vs closed-form solution, *Comput. Eng. Phys. Model.*, vol. 5, no. 4, pp. 23-50, 2022, doi: 10.22115/cepm.2023.354941.1219.

[41] Airport Engineering Division AAS, AC 150/5370-10H, Standard Specifications for Construction of Airports, 21 December 2018 (updated by errata 19 August 2020), Aug. 2020. [Online]. Available: `http://www.faa.gov/airports/aip/procurement/`

[42] K. Tuleubekov and D. R. Brill, Correlation between Subgrade Reaction Modulus and CBR for Airport Pavement Subgrades, in *T&DI Congress*, 2014, pp. 813-822.

[43] C. Caliendo and A. Parisi, Stress-prediction model for airport pavements with jointed concrete slabs, *J. Transp. Eng.*, vol. 136, no. 7, pp. 664-677, 2010, doi: 10.1061/(ASCE)TE.1943-5436.0000151.

[44] American Association of State Highway and T. O. (AASHTO), AASHTO Guide for Design of Pavement Structures, Washington, D.C., 1993. [Online]. Available: `https://bookstore.transportation.org/`

[45] Portland Cement Association (PCA), Thickness Design for Concrete Highway and Street Pavements, Skokie, IL, 1984. [Online]. Available: `https://www.cement.org/`

[46] Portland Cement Association (PCA), Thickness Design for Concrete Highway and Street Pavements, Skokie, IL, 1984. [Online]. Available: `https://www.cement.org/`

[47] H. Li, S. Sen, and L. Khazanovich, "A scalable adaptive sampling approach for surrogate modeling of rigid pavements using machine learning," *Results in Engineering*, vol. 23, Sep. 2024, doi: 10.1016/j.rineng.2024.102483.

Declaration of interests

☒ The authors declare that they have no known competing financial interests or personal relationships that could have appeared to influence the work reported in this paper.

☐ The authors declare the following financial interests/personal relationships which may be considered as potential competing interests: